Physics in Medicine & Biology

PAPER • **OPEN ACCESS**

A fast analytical dose calculation approach for MRI-guided proton therapy

To cite this article: Alisha Duetschler *et al* 2023 *Phys. Med. Biol.* **68** 195020

IOP Publishing Phys. Med. Biol. 68 (2023) 195020 https://doi.org/10.1088/1361-6560/acf90d

Physics in Medicine & Biology

IPEM Institute of Physics and Engineering in Medicine

OPEN ACCESS

RECEIVED
8 May 2023

REVISED
15 August 2023

ACCEPTED FOR PUBLICATION
12 September 2023

PUBLISHED
26 September 2023

PAPER

A fast analytical dose calculation approach for MRI-guided proton therapy

Alisha Duetschler[1,2], Carla Winterhalter[1], Gabriel Meier[1], Sairos Safai[1], Damien C Weber[1,3,4], Antony J Lomax[1,2] and Ye Zhang[1,*]

[1] Center for Proton Therapy, Paul Scherrer Institute, 5232 Villigen PSI, CH, Switzerland
[2] Department of Physics, ETH Zürich, 8092 Zürich, CH, Switzerland
[3] Department of Radiation Oncology, University Hospital of Zürich, 8091 Zürich, CH, Switzerland
[4] Department of Radiation Oncology, Inselspital, Bern University Hospital, University of Bern, 3010 Bern, CH, Switzerland
[*] Author to whom any correspondence should be addressed.

E-mail: ye.zhang@psi.ch

Keywords: MR-guidance, proton therapy, dose calculation

Abstract

Objective. Magnetic resonance (MR) is an innovative technology for online image guidance in conventional radiotherapy and is also starting to be considered for proton therapy as well. For MR-guided therapy, particularly for online plan adaptations, fast dose calculation is essential. Monte Carlo (MC) simulations, however, which are considered the gold standard for proton dose calculations, are very time-consuming. To address the need for an efficient dose calculation approach for MRI-guided proton therapy, we have developed a fast GPU-based modification of an analytical dose calculation algorithm incorporating beam deflections caused by magnetic fields. *Approach.* Proton beams (70–229 MeV) in orthogonal magnetic fields (0.5/1.5 T) were simulated using TOPAS-MC and central beam trajectories were extracted to generate look-up tables (LUTs) of incremental rotation angles as a function of water-equivalent depth. Beam trajectories are then reconstructed using these LUTs for the modified ray casting dose calculation. The algorithm was validated against MC in water, different materials and for four example patient cases, whereby it has also been fully incorporated into a treatment plan optimisation regime. *Main results.* Excellent agreement between analytical and MC dose distributions could be observed with sub-millimetre range deviations and differences in lateral shifts <2 mm even for high densities (1000 HU). 2%/2 mm gamma pass rates were comparable to the 0 T scenario and above 94.5% apart for the lung case. Further, comparable treatment plan quality could be achieved regardless of magnetic field strength. *Significance.* A new method for accurate and fast proton dose calculation in magnetic fields has been developed and successfully implemented for treatment plan optimisation.

1. Introduction

Pencil beam scanned (PBS) proton therapy can reduce the dose to nearby organs at risk (OARs) (Lomax *et al* 1999a) compared to conventional photon radiotherapy, due to the concentrated dose deposition in the Bragg peak (Bragg and Kleeman 1905). However, for the same reason, protons are very sensitive to differences in the patient's setup and internal anatomy changes, which makes it difficult to guarantee the precise location of the Bragg peak within the tumour volume. Thus, accurate online image guidance is very important to exploit the full potential of proton therapy.

Magnetic resonance imaging (MRI) is a non-ionizing imaging modality and provides excellent soft-tissue contrast. Integrating MRI into the treatment process enables real-time visualization of the tumour and surrounding anatomy, allowing for more precise dose delivery. While for MR-guided photon therapy, two commercial systems are in clinical use (Mutic and Dempsey 2014, Raaymakers *et al* 2017), MR-guided proton therapy is just beginning to be investigated (Oborn *et al* 2017, Hoffmann *et al* 2020, Pham *et al* 2022) with proof

of concept and first experimental results having been recently reported using experimental systems (Schellhammer *et al* 2018a, 2018b, Lühr *et al* 2019, Padilla-Cabal *et al* 2019, Gantz *et al* 2020, 2021, Fuchs *et al* 2022).

In contrast to photons, the magnetic field of the MR imaging system causes a deflection of the primary proton beam due to its charged nature. Therefore, the impact of the magnetic field on proton beams and its consequent effect on dose distributions has been investigated in various simulation studies using Monte Carlo (MC) simulations (Raaymakers *et al* 2008, Moteabbed *et al* 2014, Oborn *et al* 2015, Fuchs *et al* 2017, Lühr *et al* 2019, Santos *et al* 2019). Several correction strategies were proposed to account for the deflection of proton beams (Moteabbed *et al* 2014, Hartman *et al* 2015, Oborn *et al* 2015, Schellhammer and Hoffmann 2017, Burigo and Oborn 2019, 2021). Furthermore, studies utilising MC-based treatment planning have demonstrated the feasibility of achieving comparable plan quality in magnetic fields of MR scanners (Hartman *et al* 2015, Kurz *et al* 2017, Burigo and Oborn 2019, 2021).

Although MC is widely considered as the most accurate method for dose calculation in radiation therapy, it requires long computation times. For this reason, analytical algorithms could have advantages in MR-guided proton therapy, where short dose calculation and optimisation times become especially important for online plan adaptations (Matter *et al* 2019, Nenoff *et al* 2020). To this end, several methods have been proposed for analytically or numerically estimating the deflection of proton beams in a perpendicular magnetic field (Wolf and Bortfeld 2012, Hartman *et al* 2015, Fuchs *et al* 2017, Schellhammer and Hoffmann 2017). As full analytical dose calculations, however, only two pencil beam algorithms have so far been presented by Padilla-Cabal *et al* (2018, 2020a). Based on MC calculations in water, a specific parametrisation of the deflected beam using a Gaussian with exponential tails (Padilla-Cabal *et al* 2018) or a double Gaussian fitting model (Padilla-Cabal *et al* 2020a) has been established. In the case of materials other than water, a look-up based on water-equivalent depth was performed. However, different materials cause different beam trajectories in a magnetic field. To account for this, a material-specific correction factor was incorporated in the former algorithm (Padilla-Cabal *et al* 2018). The application of material-specific correction factors is, however, impractical in the case of real patient CTs. Consequently, no correction factors were used anymore in the second implementation (Padilla-Cabal *et al* 2020a), which could result in substantial differences in materials other than water. This second analytical dose calculation algorithm (Padilla-Cabal *et al* 2020a) was further integrated into a research treatment planning system and used for plan optimisation in the presence of a magnetic field.

Accurate and efficient methods for dose calculation and treatment planning considering the impact of magnetic fields on proton beams are important for the future implementation of MR-guided proton therapy. We have previously reported on a fast analytical dose calculation for proton therapy and its performance in relation to MC calculations (Winterhalter *et al* 2019a) and also on an extension of this algorithm to work with a deforming dose grid for 4D dose calculations (Van De Water *et al* 2009, Boye *et al* 2013a, Krieger *et al* 2018). Based on these, in this work, we have developed a novel fast analytical dose calculation approach which effectively accounts for proton beam deflections in a magnetic field. Our approach is a modification of the ray casting algorithm (Schaffner *et al* 1999), which is used clinically at our institute and has been accelerated by using graphics processing units (GPUs) (Matter *et al* 2019). The new algorithm has been benchmarked in water and different materials against MC calculations for different magnetic field strengths. In addition, it has been incorporated into an optimisation regime whereby fields and plans can be fully optimised in the presence of magnetic fields. As proof of principle, treatment plans have been generated for four patient cases with different tumour indications and anatomical sites and the resulting doses compared to MC simulations.

2. Materials and methods

2.1. Dose calculation algorithm

In the absence of a magnetic field, the dose deposited at a point $\vec{x}^0 = (x^0, y^0, z^0)$ by a single pencil beam with initial energy E_0 and position $(x^{\text{beam}}, y^{\text{beam}})$ can be calculated using ray casting (Schaffner *et al* 1999) as:

$$\begin{aligned}&\mathfrak{D}(\vec{x}^0) = \mathrm{N}_{p^+}\mathrm{ID}(\mathrm{WED}^0)\frac{1}{2\pi\sigma_x\sigma_y}\exp\left(-\frac{(x^{\text{beam}}-x^0)^2}{2\sigma_x^2}\right)\exp\left(-\frac{(y^{\text{beam}}-y^0)^2}{2\sigma_y^2}\right),\\&\text{where } \mathrm{WED}^0 = \mathrm{WED}^0(\vec{x}^0)\\&\text{and } \sigma_i = \sigma_i(E^0, \mathrm{WED}^0(\vec{x}^0)) \text{ with } i = x, y.\end{aligned} \tag{1}$$

N_{p^+} is the number of protons, ID is the integral depth dose dependent on the initial beam energy and energy spectrum and WED^0 is the water-equivalent depth of the point $\vec{x}^0$. The dose of a pencil beam is modelled using a single Gaussian in both lateral directions with standard deviations of σ_x and σ_y.

This approach has been modified to account for the deflection of proton beams in magnetic fields. First, based on trajectories of proton pencil beams in water as observed in MC dose calculations (section 2.1.1), a

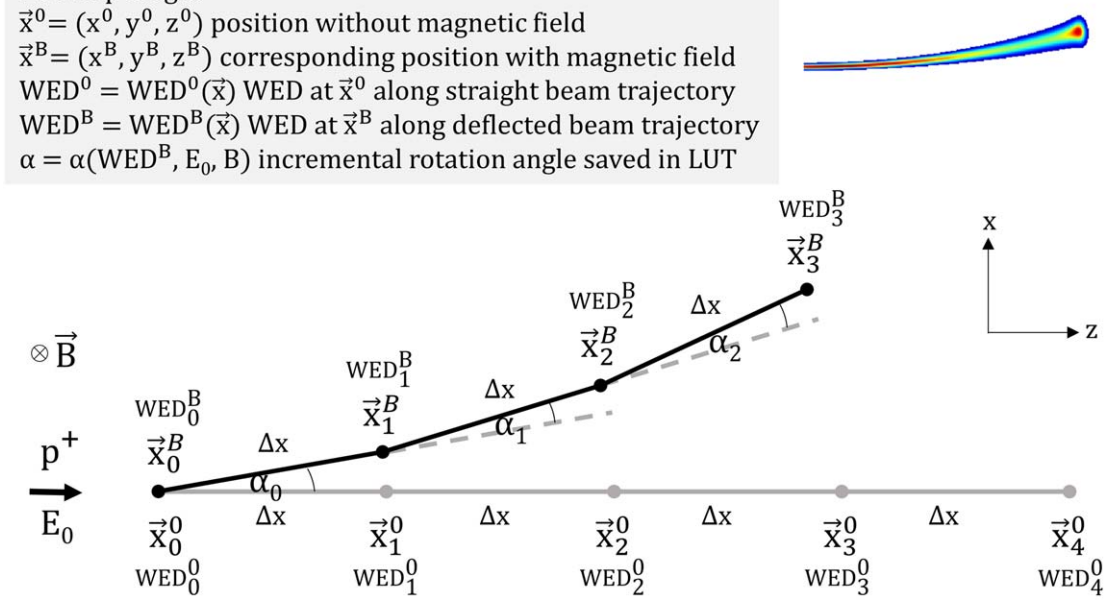

Figure 1. Schematic of deflected beam trajectory based on incremental rotation angles. An example beam is shown at the top right.

trajectory correction method based on look-up tables (LUT) of incremental rotation angles has been developed (section 2.1.2). Second, the dose calculation engine has been modified for dose deposition along these deflected trajectories (section 2.1.3).

2.1.1. Generation of LUTs from Monte Carlo beam trajectories

All MC calculations were performed using TOPAS version 3.5.0 (Tool for particle simulations) (Perl *et al* 2012, Faddegon *et al* 2020), which is based on GEANT4 (version 10.06.p01) (Agostinelli *et al* 2003, Allison *et al* 2006, 2016). Using a previously established beam model (Winterhalter 2019), proton beams of the 115 clinical energies (70–229 MeV) of PSI-Gantry2 were simulated starting 47.8 cm upstream of the isocentre (along *z*-axis). The dose distributions were scored in a rectangular water phantom using voxels of 0.1 mm (lateral displacement) × 5 mm × 0.5 mm (depth dose). The size of the water phantom was varied depending on the energy to reduce computation times and fully stop the beam (lowest energy: $5 \times 5 \times 12$ cm^3; highest energy: $20 \times 5 \times 35$ cm^3). Simulations without magnetic field (0 T) and with uniform, perpendicular magnetic fields (along $-y$-axis) of 0.5 and 1.5 T within the water phantom were performed, with 10^7 protons for each simulation.

From the resulting MC dose distributions, the beam centre is extracted using Gaussian fitting and smoothing. Making steps of fixed length (Δx) along the deflected beam centre trajectory, an incremental rotation angle α_i is calculated for each step ($i = 0, 1, 2, \ldots$) (see figure 1). These incremental rotation angles are then stored in a LUT for each energy E_0 and magnetic field strength B.

2.1.2. Beam trajectory calculation in heterogeneous media

For in-patient dose calculations, the deflected beam trajectory in heterogeneous media has to be determined. Using a small step length and assuming constant energy over each step, the residual energy of the proton beam determines the gyro-radius in each step. Using a different parameterisation, the incremental rotation angle α_i is determined by the initial energy E_0 and water-equivalent depth WED_i^B of a point $\vec{x}_i^{\,B}$ along a deflected beam trajectory. While the LUTs of α as a function of WED were generated from simulations in water, due to the considerations above, the method also applies to other materials and the effects of heterogeneities in the beam path are considered. Thus, the beam path can be iteratively calculated as illustrated in figure 1.

However, for air, the energy loss is neglected ($\mathrm{WED}_{\mathrm{air}} = 0$), which results in a constant $\alpha_{\mathrm{air}} = \alpha_0$ in each step, eventually leading to a circular path. While the above-described method conceptually also works for air, errors in the very small α_0 accumulate, which can lead to more pronounced differences compared to other materials. In the air around the patient, the incremental rotation angle α_{air} is therefore calculated analytically using a small-angle approximation for each energy E_0 from the relativistic gyro-radius r as

$$\alpha_{\text{air}} = 2\arcsin\left(\frac{\Delta z}{2r}\right) \text{with } r = \frac{\sqrt{2m_p E_0\left(1 + \frac{E_0}{2m_p c^2}\right)}}{qB}, \tag{2}$$

where m_p is the mass of a proton, q the charge of the proton and c is the speed of light. With this, a sub-millimetre accuracy in the lateral displacement compared to MC was observed even after 30 cm of air.

2.1.3. Modified ray casting algorithm for proton beams in a magnetic field

The dose calculation requires a calculation of the WED, which is typically calculated on a regular calculation grid. To consider the impact of the magnetic field, for each energy, the calculation grid is deformed according to the trajectory calculation method described in the previous section and WED^B is calculated along the deformed trajectories, similarly to the deforming dose grid algorithm for 4D dose calculation (Van De Water *et al* 2009, *et al* 2013b, Krieger *et al* 2018). Accordingly, WED^B is saved for points $\vec{x}^B = (x^B, y^B, z^B) = (x^0 + \Delta_{\text{lat}}, y^0, z^0 + \Delta_{\text{dist}})$ shifted by a distal (Δ_{dist}) and lateral (Δ_{lat}) displacement for each grid point $\vec{x}^0 = (x^0, y^0, z^0)$.

For each point $\vec{x}^B$, the dose is then calculated as:

$$\begin{aligned} \mathfrak{D}(\vec{x}^B) = {} & \text{N}_p \text{ID}(\text{WED}^B)\frac{1}{2\pi\sigma_x\sigma_y}\exp\left(-\frac{(x^{\text{beam}} - x^0)^2}{2\sigma_x^2}\right)\exp\left(-\frac{(y^{\text{beam}} - y^0)^2}{2\sigma_y^2}\right), \\ & \text{with } \text{WED}^B = \text{WED}^B(\vec{x}^B) \\ & \text{and } \sigma_i = \sigma_i(E^0, \text{WED}^B(\vec{x}^B)) \text{ with } i = x, y. \end{aligned} \tag{3}$$

Note, that while the integral depth dose ID and the standard deviations σ are now determined based on the modified WED^B, the corresponding original grid point (x^0, y^0) is used to calculate the Gaussian functions. Finally, the dose is linearly distributed to the nearest points on the original regular grid based on the displacement $(\Delta_{\text{lat}}, \Delta_{\text{dist}})$ of the centre of each pencil beam.

2.2. Treatment planning in magnetic fields

For this proof of concept treatment planning study, an implementation of the MR-compatible dose calculation algorithm described above was further used to calculate the dose influence matrix for subsequent plan optimisation. In the conventional 0 T case, spots are placed within the target on a regular grid with lateral spacing of 4 mm and spacing between energy layers of 2.5 mm. Prior to the optimisation with magnetic field, however, a spot-shifting approach needs to be applied.

This is done using an energy-specific spot-shifting method and further discarding spots located outside of the target. For each field direction and energy layer, the lateral displacement (Δ_{lat}) just after the Bragg peak ($R_{80\%}$) was determined for a central beam directed at the isocentre according to the trajectory calculation method described previously. For each energy layer, spots were then shifted in the opposite direction, which could be achieved using a parallel scanning capability. In initial evaluations of this spot-shifting method, the target coverage of plans optimised without a magnetic field could not be restored even with an additional margin added to the planning target volume (PTV), due to heterogeneities and different amounts of air before entering the patient. Therefore, each field needs re-optimisation. For this, the updated dose influence matrix, which considers the effects of the magnetic field, was used as input into the same spot weight optimiser as used in our clinical treatment planning system (Lomax 1999b, Matter *et al* 2019).

2.3. Software implementation

The above described dose calculation and optimisation strategies were implemented in Java (Oracle Corporation, Redwood Shores, CA, USA) and incorporated into a research version of our in-house treatment planning system FIonA. The code is accelerated using dedicated GPU Aparapi kernels (Khronos Group, Beaverton, OR, USA). Calculations were performed on a NVIDIA Quadro P2200 (Nvidia Corporation, Santa Clara, CA, USA).

2.4. Benchmarking of the algorithm for single pencil beams in homogeneous media

The analytical dose calculation was thoroughly validated for individual pencil beams in a water phantom ($40 \times 30 \times 10$ cm^3) through comparison to TOPAS MC results. Analytical and MC dose calculations for all energies and magnetic field strength of 0, 0.5 and 1.5 T have been performed and compared.

Further, for the lowest, intermediate and highest energies (70, 170 and 229 MeV) the difference in beam bending and range $R_{80\%}$ in different homogeneous materials was also analysed. The dose in homogeneous phantoms mimicking lung tissue (−700 HU), adipose tissue (−100 HU), soft tissue (200 HU), cancellous bone (300 HU) and cortical bone (1000 HU) was simulated. For all benchmarking phantom simulations of individual pencil beams, the magnetic field was restricted to the phantom geometry. The results are presented in the appendix A.

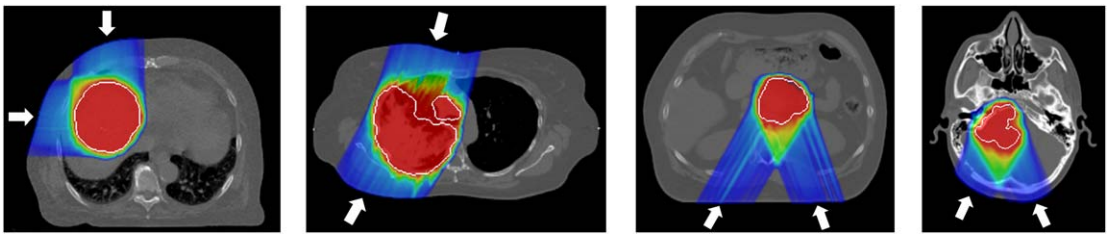

(a) Liver (b) Lung (c) Pancreas (d) Skull

Figure 2. Planned dose distributions without magnetic field (0 T) for all four patient cases. White arrows indicate the field directions and the PTV is delineated in white.

2.5. Dose comparisons for treatment plans

Treatment plans were optimised first for a sphere (radius = 5 cm, depth = 25 cm) in the water phantom without a magnetic field (0 T) and then in the presence of a 0.5 and 1.5 T magnetic field as described in section 2.2. For each plan, the dose was calculated analytically and compared against MC simulations. Further, treatment plans for four patient cases of various indications were each optimised for the three magnetic field strengths. The resulting optimised treatment plans were then recalculated using TOPAS MC with statistical uncertainties below 1%.

Each field dose distribution was normalised to a mean dose to the PTV of 100%. The resulting dose distributions were then compared in terms of dose differences and global gamma pass rate with an absolute dose difference of 2% and 2 mm distance to agreement using a lower 1% dose threshold. The effects on the plan quality were evaluated through the use of dose–volume histograms (DVHs) for the PTV and surrounding organs. In addition, the PTV dose coverage $V_{95\%}$ and homogeneity $D_{5\%}$–$D_{95\%}$ were assessed.

2.6. Patient data and treatment planning parameters

As proof of principle tests of the developed approach, treatment plans have been optimised for a water phantom and for liver, lung, pancreas and skull base patient cases. Simplified treatment plans with two field directions (1 field for water phantom) were optimised using a single-field uniform-dose (SFUD) approach. The same field directions, as visualised in figure 2, were used with and without magnetic fields. Further, the same optimisation objectives were selected for all three magnetic field strengths to assess the performance of the optimisation algorithm.

To simulate the placement of a patient in the magnetic field of an MRI scanner, a homogeneous magnetic field within a cylinder around the isocentre was assumed for all treatment plan dose calculations and optimisations. A radius of 35 cm was used, which corresponds to the bore radius of both MR-linac systems currently in use. Consequently, the bending of the proton beam in the air around the patient leads to a different beam entrance angle for 0.5 and 1.5 T compared to 0 T. No fringe fields were simulated.

For all analytical dose calculations, the clinically used beam model of PSI-Gantry2 (Pedroni *et al* 2004, Zenklusen *et al* 2010, Safai *et al* 2012) was used. For the analytical dose calculations of treatment plans, a dose calculation grid of 2.5 mm × 4 mm (lateral) × 2.5 mm (distal) was used, with a smaller spacing in the two axes affected by the magnetic field. The dose was then linearly interpolated onto the CT voxels. In contrast, the dose was directly scored in the voxels of the CT when using MC.

3. Results

3.1. Water phantom

The treatment plans for the spherical target in the water phantom optimised in the presence of different magnetic field strengths are shown in figure 3. A lateral offset of the beam when entering the water phantom of roughly 1.5 cm and 4 cm for 0.5 T and 1.5 T, respectively, can be observed compared to the 0 T scenario. The dose differences between the analytical and MC dose results are only slightly larger with magnetic fields than in the 0 T scenario and dose differences are mostly concentrated in the lateral penumbra due to the single Gaussian beam model. Dose differences distal to the target occur due to small differences in range, which are also caused by energy loss in air before the phantom, which is not taken into account in analytical dose calculations. Excellent 2%/2 mm gamma pass rates were achieved, with only a minimal reduction for the highest magnetic field strength 1.5 T (98.9%) compared to the 0 T (99.2%) scenario (see table 1).

DVHs of the target for the three magnetic field strengths calculated analytically and with MC are shown in figure 4. A very slight overestimation of the target coverage as well as a slightly higher overdosage by the analytical

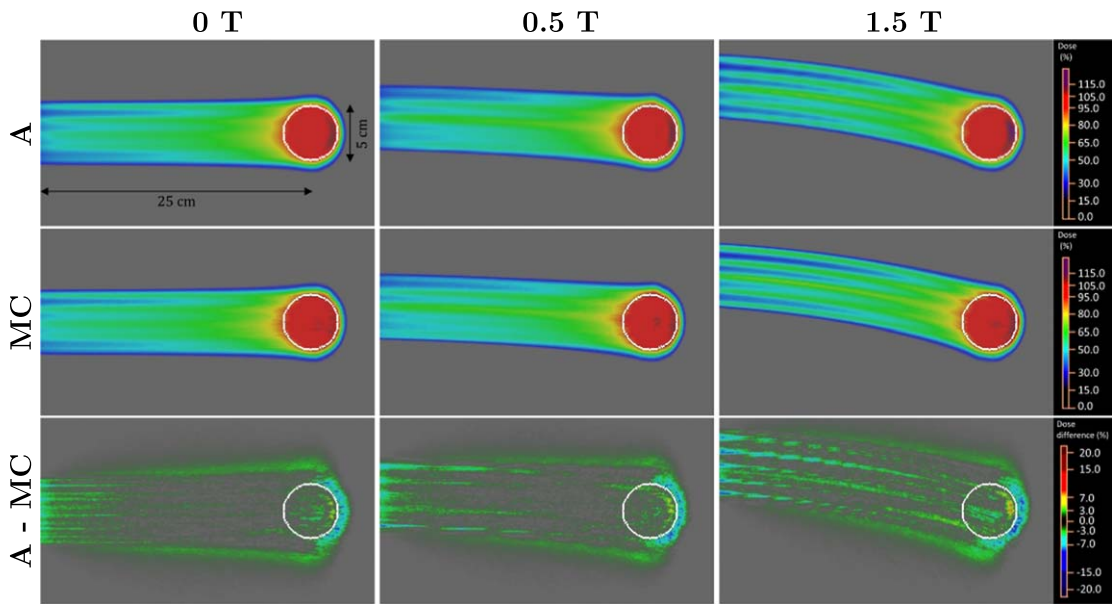

Figure 3. Treatment plan for spherical target in water optimised for 0 T (left), 0.5 T (centre) and 1.5 T (right). Dose distributions calculated analytically (top), with TOPAS-MC (middle) and their difference (bottom) are shown.

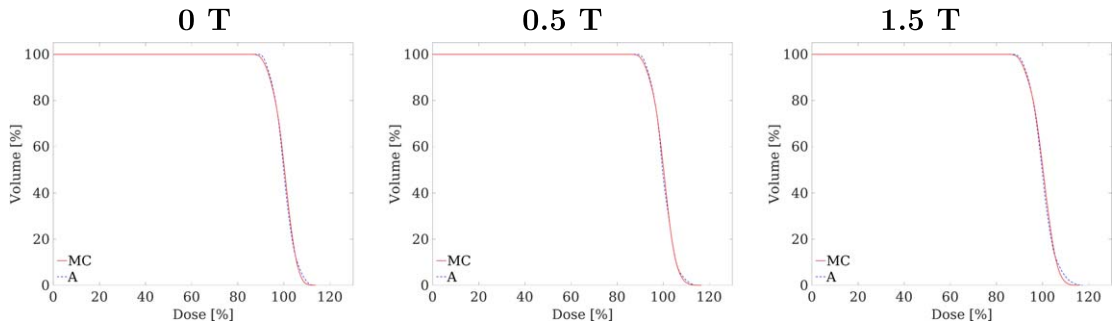

Figure 4. DVHs for spherical target in water for 0 T (left), 0.5 T (centre) and 1.5 T (right). Results for MC (red line) and analytical (dashed blue line) dose calculation are shown.

Table 1. Comparison analytical (A) and MC results for spherical target in water for different magnetic field strength. 2%/2 mm gamma pass rate and DVH parameters of the PTV are listed [%].

	0 T		0.5 T		1.5 T	
	A	MC	A	MC	A	MC
Gamma pass rate	99.2		99.3		98.9	
PTV $V_{95\%}$	86.3	85.6	86.2	85.7	84.4	84.1
PTV $D_{5\%}$–$D_{95\%}$	15.2	14.9	15.0	15.2	17.1	16.2

algorithm compared to MC can be observed. However, $V_{95\%}$ of the PTV agrees within 0.7% and $D_{5\%}$–$D_{95\%}$ within 0.9% for all three scenarios (see table 1). Comparable plan quality is obtained for all three magnetic field strengths, with only a small degradation of 1.9% in $V_{95\%}$ and $D_{5\%}$–$D_{95\%}$ in the analytical plan when a magnetic field of 1.5 T is introduced.

For this phantom case, the optimisation including final dose calculation, both considering the magnetic field, was completed in less than 30 s.

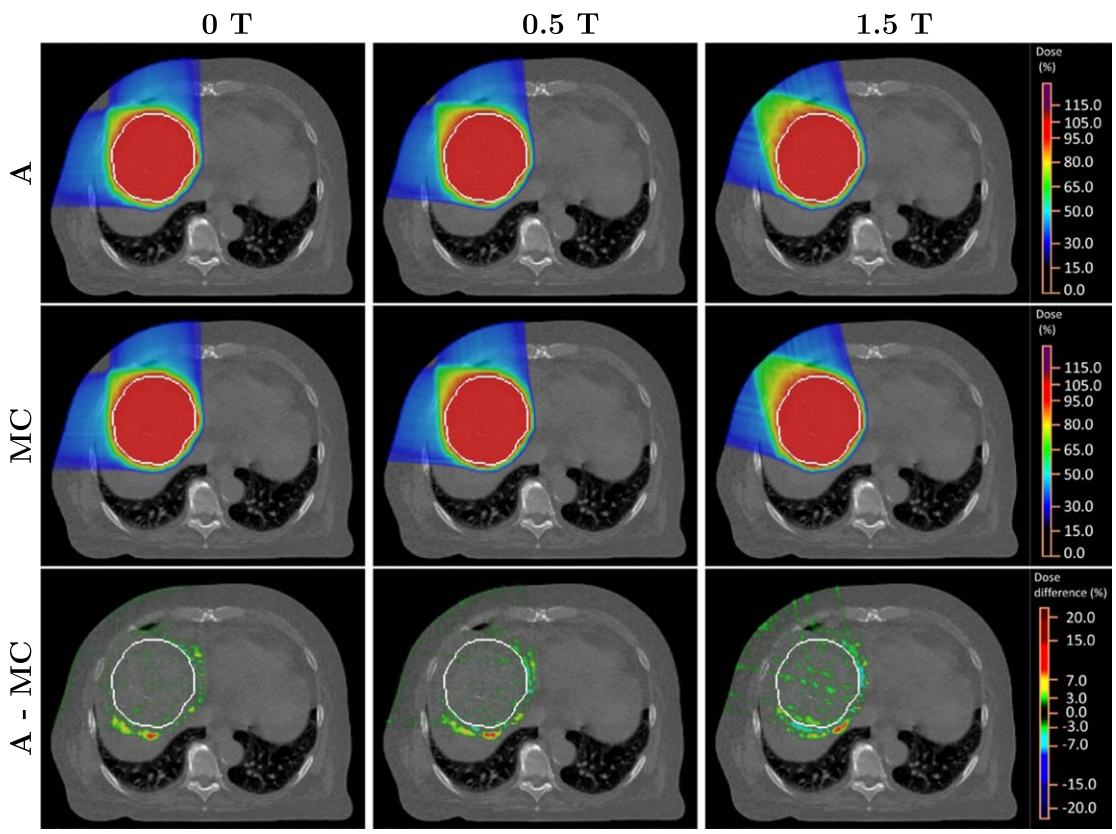

Figure 5. Treatment plan for liver case optimised for 0 T (left), 0.5 T (centre) and 1.5 T (right). Dose distributions calculated analytically (top), with TOPAS-MC (middle) and their difference (bottom) are shown.

3.2. Patient cases

Dose distributions for the four clinical cases are shown in figures 5–8. For the liver case (figure 5), dose differences are mostly concentrated distal to the tumour, with only a small increase with increasing magnetic field strength. Overall, 94.5% and 90.9% of voxels receiving a dose greater than 1% of the prescription dose have an absolute dose difference smaller than 3% ($V_{\text{dosediff}>3\%}$) for 0 T and 1.5 T, respectively. It should be noted that although the same field directions (i.e. the same gantry angles) were used for the treatment plans optimised for the different magnetic field strengths, there is an apparent difference in field direction due to the lateral spot shifting and deflection of the beams in air around the patient. Larger differences occur for the highly heterogeneous lung case (figure 6) with a decrease of $V_{\text{dosediff}>3\%}$ with increasing magnetic field strength (0 T: 83.1%, 0.5 T: 78.8% and 1.5 T: 73.2%). Most pronounced dose differences occur in the low density lung tissue. Dose distributions and dose differences for the pancreas case in figure 7 again show most pronounced dose differences distal to the target for 0 T and 0.5 T, with $V_{\text{dosediff}>3\%}$ of 96.8% and 94.0%, respectively. For the higher magnetic field strength, increased dose differences also occur in the beam path, resulting in $V_{\text{dosediff}>3\%}$ of 91.3%. Further, some dose hot spots in the target for 1.5 T are visible especially when calculated using MC. For the skull base case (figure 8), dose differences are also mostly located distal to the target, with some increased dose differences for 1.5 T due to greater tissue density heterogeneities. $V_{\text{dosediff}>3\%}$ of 95.2%, 93.7% and 92.6% were obtained for the three magnetic field strengths.

The 2%/2 mm gamma pass rates between the analytical and MC dose distributions for all four example cases are listed in table 2. Very high gamma pass rates above 96% were achieved for the pancreas, liver and skull case with comparable pass rates for no magnetic field and a low magnetic field 0.5 T. On average, slightly lower (1.4%) gamma pass rates were obtained for 1.5 T for these three cases. The lung case resulted in generally lower gamma pass rates also without magnetic field (92.2%) and especially for 1.5 T (81.3%). This could be explained by the low-density lung tissue and pronounced density heterogeneities in this area.

DVHs for the PTV and a selection of OARs are illustrated in figure 9 for all cases. For the liver case, a very similar plan quality was achieved for all magnetic field strengths (top row). A very good agreement also in terms of DVHs can be observed between the analytical and MC results, which is also reflected by the differences in the target coverage $V_{95\%}$ below half a percent (see table 3). The PTV $D_{5\%}$–$D_{95\%}$ homogeneity is slightly overestimated by the analytical calculation by around 1%. For the lung case, the largest dosimetric differences in the PTV dose coverage and homogeneity were actually observed for the case without magnetic field. A good

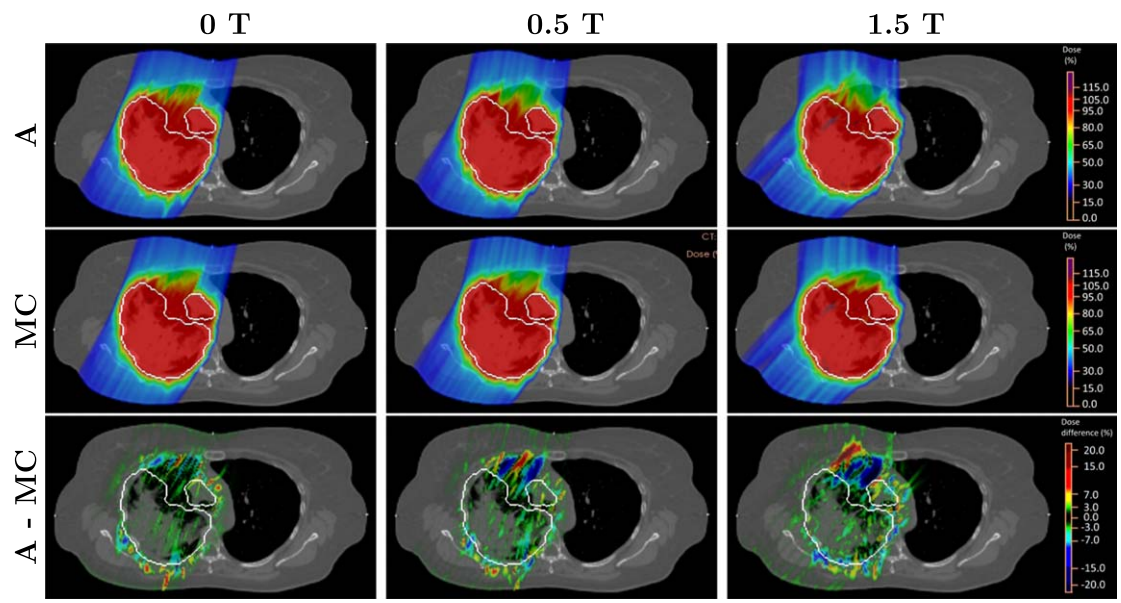

Figure 6. Treatment plan for lung case optimised for 0 T (left), 0.5 T (centre) and 1.5 T (right). Dose distributions calculated analytically (top), with TOPAS-MC (middle) and their difference (bottom) are shown.

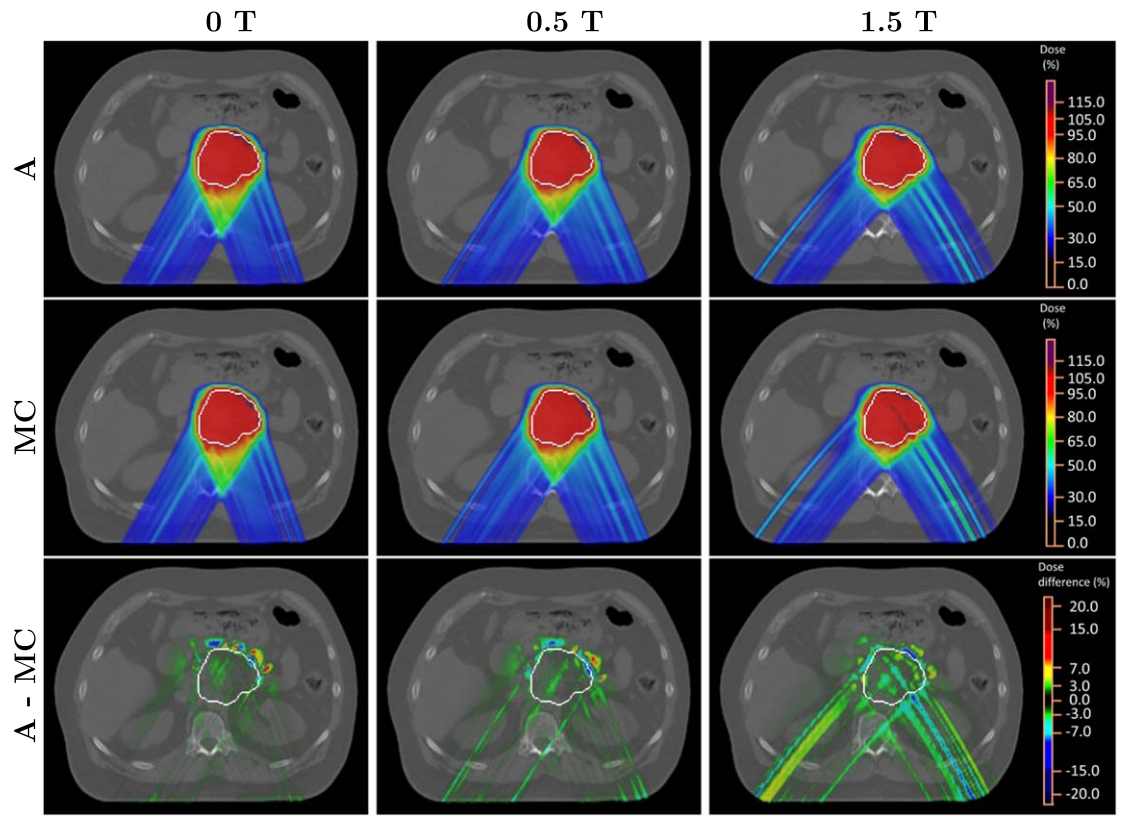

Figure 7. Treatment plan for pancreas case optimised for 0 T (left), 0.5 T (centre) and 1.5 T (right). Dose distributions calculated analytically (top), with TOPAS-MC (middle) and their difference (bottom) are shown.

agreement in the DVHs between the analytical algorithm and MC can also be observed for the pancreas case. DVHs for the PTV and a selection of OARs for the skull case are displayed at the bottom of figure 9. The PTV dose coverage and homogeneity is very slightly overestimated by the analytical dose calculation for 0 T and 0.5 T and very similar for 1.5 T. Most pronounced dosimetric differences can be observed in the right cochlea (cyan) and middle ear (green), which are located in the area of the largest dosimetric uncertainties distal to the PTV. For

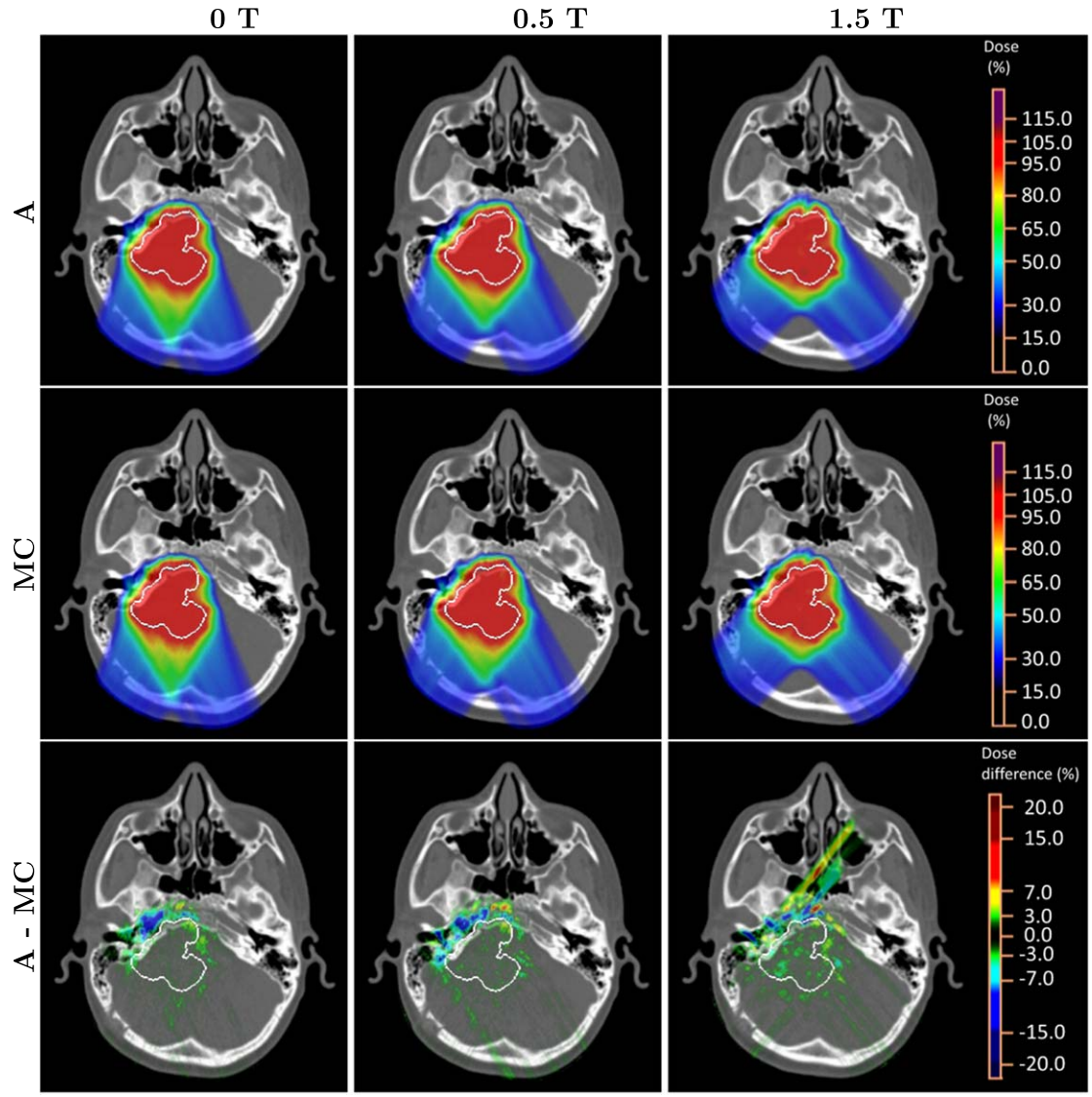

Figure 8. Treatment plan for skull case optimised for 0 T (left), 0.5 T (centre) and 1.5 T (right). Dose distributions calculated analytically (top), with TOPAS-MC (middle) and their difference (bottom) are shown.

Table 2. 2%/2 mm gamma pass rates between analytical and MC dose distributions for the four patient cases [%].

	0 T	0.5 T	1.5 T
Liver case	96.9	96.7	94.5
Lung case	92.2	88.2	81.3
Pancreas case	98.5	98.7	98.0
Skull case	99.7	99.7	98.4

example, $D_{2\%}$ to the right middle ear is underestimated by the analytical calculation by 12% for 0.5 T and 4.5% for 1.5 T. A similar underestimation by 6.7%, however, also occurs in the case without magnetic field.

For all four patient cases, the observed differences in the studied DVH parameters in table 3 are comparable, for both magnetic field strengths, to the benchmarking scenario without a magnetic field.

Comparing the plan quality for the different magnetic field strengths, a slight decrease in PTV coverage and homogeneity with increasing magnetic field strength can be observed. The decrease in the PTV coverage $V_{95\%}$ is mostly due to the normalization of all treatment plans to the same mean target dose, as the optimisation, especially with a 1.5 T magnetic field, could result in some hot spots in the target. This was most pronounced for the pancreas case and is reflected by the highest PTV $D_{5\%}$–$D_{95\%}$ occurring for this case (17.1% for 1.5 T). For the

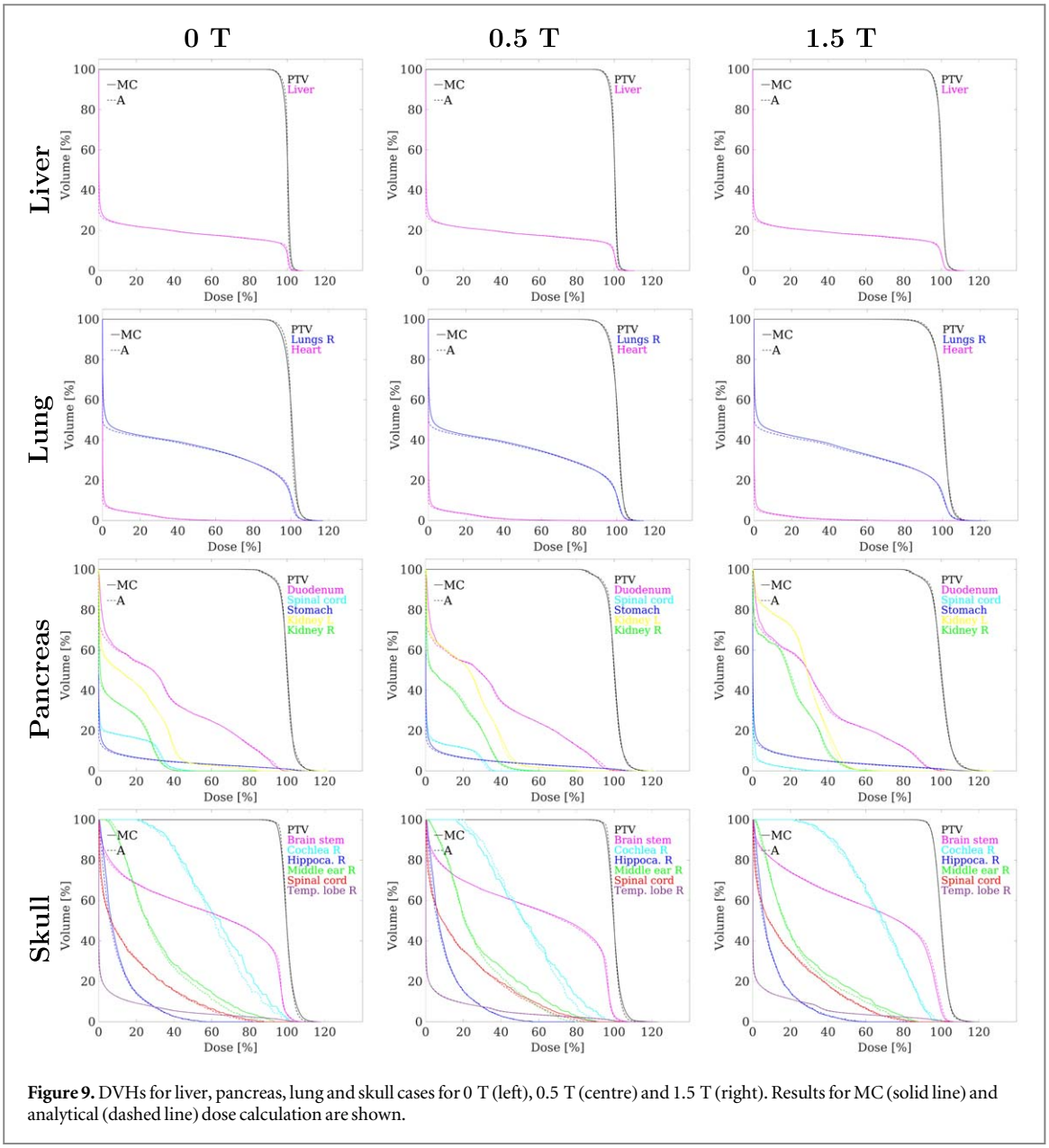

Figure 9. DVHs for liver, pancreas, lung and skull cases for 0 T (left), 0.5 T (centre) and 1.5 T (right). Results for MC (solid line) and analytical (dashed line) dose calculation are shown.

pancreas case, pronounced differences between the different magnetic field strengths in the DVHs of the spinal cord (cyan), left (yellow) and right kidney (green) can be observed in figure 9 due to the different beam paths (see dose in figure 7). In general, differences in the DVH parameters of the OARs for 0, 0.5 and 1.5 T can, however, be explained by the different entrance angles and beam trajectories within the patient resulting from the deflections due to the magnetic field.

The analytical dose calculations with magnetic field were all performed in under 30 s per field. Optimisation times considering the magnetic field were longer, with computation times per field between 30 s (skull) and 8 min (pancreas).

4. Discussion

We have developed a fast GPU-based modification of the analytical raycasting approach for PBS proton dose calculations that accounts for the deflection of proton beams in a perpendicular magnetic field. A novel method for trajectory calculation, based on MC simulations of pencil beams in water, correctly considers heterogeneities in the beam path. By using LUTs of incremental rotation angles as a function of the water-equivalent depth, the beam deflection can be accurately calculated not only in water but also in various materials. Further, no

Table 3. DVH parameters for analytical (A) and MC dose distributions and their differences (Δ) for the four patient cases [%].

	0 T			0.5 T			1.5 T		
	A	MC	Δ	A	MC	Δ	A	MC	Δ
Liver case									
PTV $V_{95\%}$	98.2	98.0	0.2	98.2	97.8	0.4	97.4	97.2	0.2
PTV $D_{5\%}$–$D_{95\%}$	4.6	5.7	−1.1	4.9	5.9	−1.0	6.7	7.1	−0.4
Liver D_{mean}	19.1	19.3	−0.2	18.7	18.9	−0.2	18.6	18.8	−0.2
Lung case									
PTV $V_{95\%}$	95.2	92.3	2.9	93.5	92.0	1.5	90.4	89.5	0.9
PTV $D_{5\%}$–$D_{95\%}$	6.8	7.9	−1.1	10.5	10.8	−0.3	13.6	13.6	0.0
Heart $D_{2\%}$	28.8	29.6	−0.8	27.9	29.3	−1.4	18.5	21.0	−2.5
Lungs R D_{mean}	35.6	36.2	−0.6	35.4	36.1	−0.7	34.4	35.3	−0.9
Pancreas case									
PTV $V_{95\%}$	93.8	92.8	1.0	92.6	91.1	1.5	90.0	88.2	1.8
PTV $D_{5\%}$–$D_{95\%}$	12.4	12.3	0.1	13.4	13.9	−0.5	17.1	17.3	−0.2
Duodenum $D_{2\%}$	95.1	94.3	0.8	95.4	93.8	1.6	93.1	92.5	0.6
Kindey L D_{mean}	17.6	18.0	−0.4	20.5	21.0	−0.5	26.0	26.5	−0.5
Kindey R D_{mean}	9.4	9.5	−0.1	12.9	13.0	−0.1	18.8	18.9	−0.1
Spinal cord $D_{2\%}$	37.6	38.6	−1.0	32.1	33.3	−1.2	15.4	16.5	−1.1
Stomach $D_{2\%}$	81.8	83.5	−1.7	81.0	83.7	−2.7	81.5	85.8	−4.3
Skull case									
PTV $V_{95\%}$	98.0	96.0	2.0	98.1	96.7	1.4	93.2	93.5	−0.3
PTV $D_{5\%}$–$D_{95\%}$	9.0	11.1	−2.1	8.8	10.9	−2.1	11.1	11.4	−0.3
Brain stem $D_{2\%}$	101.9	101.4	0.5	100.4	101.1	−0.7	102.3	101.5	0.8
Cochlea R D_{mean}	61.1	63.3	−2.2	52.9	53.6	−0.7	66.8	67.2	−0.4
Cochlea R $D_{2\%}$	99.1	99.5	−0.4	86.9	94.8	−7.9	96.1	94.4	1.7
Hippocampus R $D_{2\%}$	42.5	42.5	0.0	42.9	43.3	−0.4	44.5	44.5	0.0
Middle ear R D_{mean}	31.1	32.6	−1.5	26.5	29.1	−2.6	24.1	25.6	−1.5
Middle ear R $D_{2\%}$	81.2	87.9	−6.7	70.3	82.3	−12.0	77.4	81.9	−4.5
Spinal cord $D_{2\%}$	72.7	75.4	−2.7	75.4	79.9	−4.5	72.7	75.6	−2.9
Temporal lobe R $D_{2\%}$	86.4	86.9	−0.5	83.7	85.7	−2.0	84.8	85.4	−0.6

material-specific correction factors, as proposed in other analytical calculations (Padilla-Cabal *et al* 2018), are needed, which are difficult to apply in highly heterogeneous patient geometries.

The algorithm has been extensively validated against TOPAS-MC simulations for individual pencil beams and treatment plans in water, different materials and patient CTs, achieving excellent agreement comparable to the clinically used ray casting algorithm (Schaffner *et al* 1999). While Padilla-Cabal *et al* (2018, 2020a) have presented two analytical pencil beam dose calculation algorithms considering magnetic fields, we have presented an alternative approach. Our algorithm has further been validated against MC simulations in heterogeneous patient CTs, while previous publications have only presented validations in geometrical phantoms.

In this work, only homogeneous magnetic fields were investigated. However, the proton pencil beam delivery will also be influenced by the heterogeneous fringe field of an MR scanner (Oborn *et al* 2015). This could be incorporated into the dose calculation and treatment planning using machine-specific LUTs (Oborn *et al* 2015, Burigo and Oborn 2019). Such spatially varying and energy-specific LUTs could, for example, be generated based on MC simulations using magnetic field maps (Burigo and Oborn 2019, Lühr *et al* 2019, Padilla-Cabal *et al* 2020a, 2020b, Fuchs *et al* 2022). Finally, experimental verifications of the dose distributions in the MR scanner should be performed.

Based on ray casting, our approach inherits the intrinsic challenges when dealing with material interfaces that can affect dose calculation accuracy. One technique to address these issues is the beam splitting technique used in many pencil beam algorithms (Schaffner *et al* 1999, Soukup *et al* 2005, Padilla-Cabal *et al* 2018, 2020a, Yang *et al* 2020), which, however, results in increased calculation times. These pencil beam decomposition algorithms are better suited to deal with superficial density heterogeneities, while the ray casting algorithm usually performs better for inhomogeneities closer to the Bragg peak, as discussed by Schaffner *et al* (1999). We have further used our clinical beam model, which is based on a single Gaussian parametrisation of the lateral dose profiles and requires fewer parameters and shorter computation times than a double Gaussian model (Pedroni *et al* 2005, Padilla-Cabal *et al* 2020a). With both a single and double Gaussian model, it is impossible to model any asymmetry in the lateral profile introduced by the magnetic field. Such an asymmetry could be modelled using a Gaussian model with exponential tails (Padilla-Cabal *et al* 2018), which would increase the number of fitting parameters. For the studied magnetic field strengths, the

lateral asymmetry is small anyway (Fuchs *et al* 2017) and was found to be negligible especially compared to the Gaussian approximation.

Furthermore, analytical ray casting or pencil beam algorithms do not consider the effect of magnetic fields on secondary electrons. For MRI-guided photon therapy, substantial dose differences at tissue-air interfaces have been reported due to electron return and electron streaming effects (Raaijmakers *et al* 2005, 2007, 2008, Oborn *et al* 2009, Hackett *et al* 2018, Park et al. 2018, Malkov *et al* 2019), for example, resulting in increased skin doses. The electron return effect was found to be much smaller for MRI-guided proton therapy (Raaymakers *et al* 2008, Fuchs *et al* 2017, Lühr *et al* 2019), due to the lower energies of secondary electrons. On the other hand, while the effect of the magnetic field on secondary electrons can be considered using MC simulations, this would require higher resolutions than used by most clinical treatment planning systems (Lühr *et al* 2019). Therefore, further investigations explicitly considering the effect of magnetic fields on secondary electrons should be performed to understand its clinical significance.

While MC simulations are widely considered the most accurate method to calculate proton dose distributions, they require considerable computation times. Dedicated MC implementations using simplified physics and running on multiple central processing units (CPUs) or GPUs have led to considerable reductions in computation times (Jia *et al* 2012, Wan Chan Tseung *et al* 2015, Souris *et al* 2016, Schiavi *et al* 2017, Lee *et al* 2022). However, to our knowledge, only one such accelerated MC can also consider the impact of magnetic fields in patients (Lysakovski *et al* 2021), the speed of which would still limit its use for inverse plan optimisation for online plan adaptations. Using our modified GPU-based ray casting approach, the dose distributions for the presented treatment plans were all calculated in less than 30 s, while the TOPAS-MC simulations required multiple hours up to days.

Excellent agreement compared to MC was observed for three out of four patients with gamma pass rates $\geqslant$94.5% also with a magnetic field up to 1.5 T. Only for the lung cancer case were larger differences observed. However, uncertainties due to motion (Duetschler *et al* 2023) and anatomical changes (Nenoff *et al* 2020) are expected to be much larger than the discrepancies seen here. Additionally, and as described by Nenoff *et al* (2021) for their online adaptive proton therapy workflow, independent offline MC re-calculations could be used for quality assurance and final dose accumulation purposes (Winterhalter *et al* 2018, 2019b, Matter *et al* 2020).

Several authors have proposed and investigated correction strategies to address the issue of target misses resulting from the deflection of proton beams due to the magnetic field (Moteabbed *et al* 2014, Hartman *et al* 2015, Oborn *et al* 2015, Schellhammer and Hoffmann 2017, Burigo and Oborn 2019, 2021). In initial assessments, we found that lateral spot-shifting and extended target margins were not sufficient to restore the target dose for complex patient anatomies. Furthermore, to exploit the full potential of MR-guided proton therapy, dedicated optimisation approaches accounting for the magnetic field will be required.

For this reason, we have integrated the dose calculation algorithm into our clinically used spot weight optimisation engine, by first implementing a spot shifting method and using our analytical dose calculation approach to calculate the dose influence matrix taking into account beam deflections in the magnetic field. A proof of concept treatment planning study has shown the potential to achieve comparable planning quality with and without magnetic field. Nevertheless, there is a tendency towards hot spots in the target, especially for higher magnetic field strengths 1.5 T. One reason is a larger difference between the estimated dose during the optimisation and the final analytically calculated dose in the presence of a magnetic field, as the dose calculation is more sensitive to differences in the location of calculation points due to the beam bending. Furthermore, the spot placement, based on the shifting of spots selected without magnetic field, results in spots which are not evenly distributed on a grid due to the energy-dependent bending and effects of density heterogeneities along the beam path. On the other hand, a dedicated spot placement approach resulting in evenly distributed spots within the whole tumour volume could improve the tumour dose coverage and homogeneity. Furthermore, the same initial weights generating a spread-out Bragg peak in the target volume for 0 T were used as a starting point for the optimisation in all scenarios. For this reason, while the same optimisation objectives were used for comparability, twice as many optimisation iterations were employed when including a magnetic field.

Finally, the same field directions (couch and gantry angles) were used with and without magnetic fields, which resulted in quite different entrance angles and beam paths within the patient in comparison to the reference (0 T) plan, degrading (or improving) the dose to OARs. This effect, however, could easily be compensated for by manually (or automatically) correcting the beam path as demonstrated by Schellhammer and Hoffmann (2017) and Burigo and Oborn (2021).

Optimisation times for the studied cases were currently between 30 s and 8 min per field, depending on the target size. However, computation times could definitely be reduced using faster hardware and with some effort spent to determine the most efficient parallelization for calculating the dose influence matrix and

appropriately reducing the optimisation grid which needed to be extended to account for the non-straight beam trajectories.

5. Conclusion

We have developed a novel analytical approach to calculate PBS proton dose distributions in perpendicular magnetic fields with high speed and accuracy. The algorithm was extensively validated against MC simulations in water, different materials and various heterogeneous patient image data sets.

Furthermore, our newly developed analytical dose calculation approach has been integrated into the treatment plan optimisation process, allowing for plan optimisations in the presence of a magnetic field. Initial treatment planning studies have shown that comparable plan quality can be achieved, which sets the foundation for future treatment planning studies of MR-guided proton therapy treatments.

Acknowledgments

This project is funded by the Swiss Cancer Research foundation (KFS-4517-08-2018). The authors thank Dr med. Barbara Bachtiary for contouring of the organs for the pancreas case.

Data availability statement

The data cannot be made publicly available upon publication because they are not available in a format that is sufficiently accessible or reusable by other researchers. The data that support the findings of this study are available upon reasonable request from the authors.

Conflict of interest

The authors report no conflict of interest.

Author contributions

AD developed, implemented and tested the algorithm, performed the computations, analysed the results and drafted the manuscript. CW provided critical inputs for developing the dose calculation approach and software support, together with GM. YZ designed the study, drafted the manuscript and supervised the project as principal investigator together with AJL, SS and DCW. All authors have read, significantly revised and approved the final manuscript.

Appendix A. Benchmarking of algorithm for single pencil beams in water

To show the full potential of our analytical dose calculation approach, a dose calculation resolution of $1 \times 1 \times 1$ mm^3 was used for the benchmarking simulations in water and other homogeneous materials. Similar results were obtained for a dose calculation resolution of $2.5 \times 2.5 \times 4$ mm^3 for the analytical calculations, which was deemed sufficient for treatment plan dose distributions.

The dose distribution of a single pencil beam with the highest energy (229 Mev) calculated analytically and with MC and their dose difference are shown in figure A1. Comparable dose differences occur with and without magnetic field and are mostly due to the single Gaussian approximation in the analytical ray casting approach. A very good agreement is also visible in the integral depth dose curve in figure A2(a), clearly showing a retraction of the Bragg peak by ~3.5 mm for 1.5 T with MC and analytically. The lateral profiles at 80% of the range in figure A2(b) show a lateral dose shift of 8 mm and 25 mm for 0.5 T and 1.5 T, respectively, with very good agreement between the analytical calculation and MC. The limitations of a single Gaussian approximation become apparent in the tails of the lateral profile, revealing known differences also without any magnetic field. These differences are already larger in the 0 T case than any beam asymmetry introduced by the magnetic field. Overall, the agreement between the analytical dose and the MC simulation is comparable for 0 T and both 0.5 T and 1.5 T.

For each energy and magnetic field strength, the range $R_{80\%}$ and the longitudinal Bragg peak width $W_{80\%}$ (80%–80%) were extracted from the integrated depth dose curve. Further, from the lateral profile at 80% of the range the beam centre x and beam width σ_x were extracted using a Gaussian fit. The difference between the

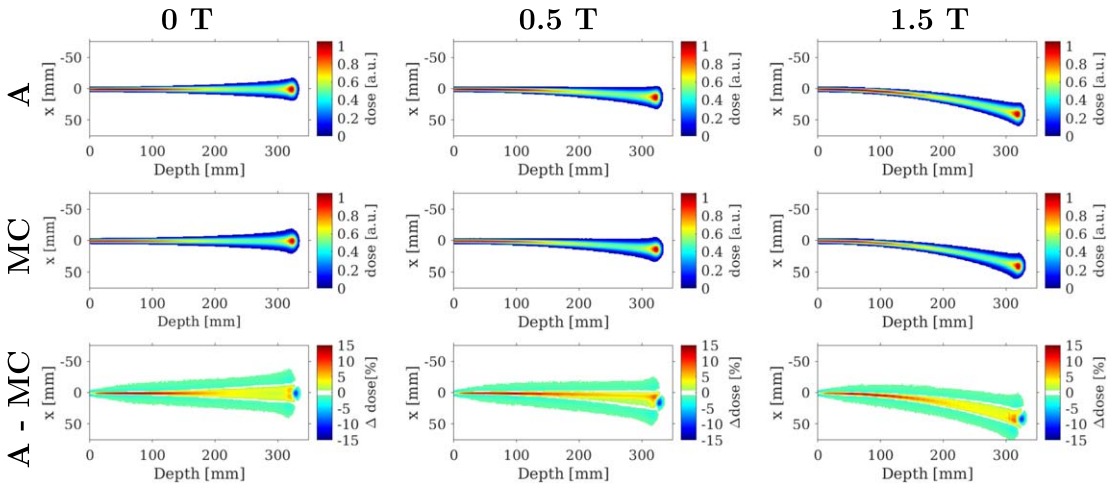

Figure A1. Dose distribution of 229 MeV pencil beam in water calculated analytically (top), with TOPAS-MC (middle) and their difference (bottom) for 0 T (left), 0.5 T (center) and 1.5 T (right). Analytical and MC doses were normalized to the same maximum dose in the integral depth dose curve for 0 T.

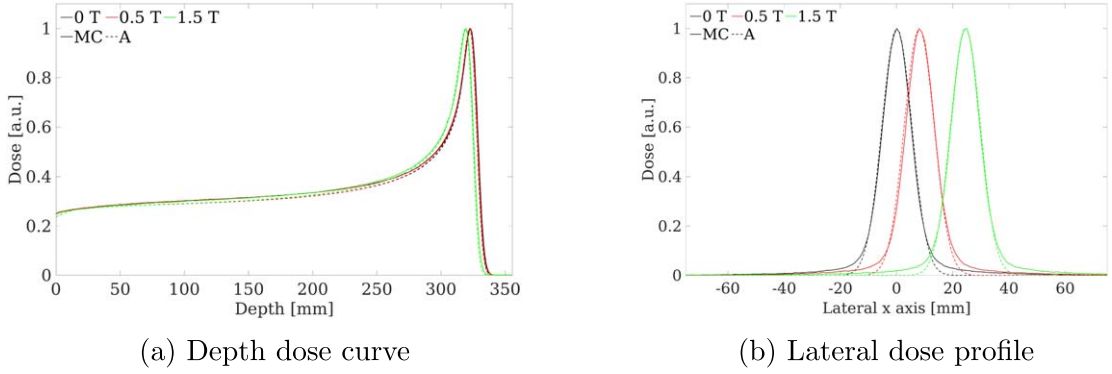

Figure A2. Depth dose curve (a) and lateral dose profile at 80% of the range $R_{80\%}$ (b) for 229 MeV pencil beam in water calculated using Monte Carlo (solid line) and analytically (dashed line) normalized to the maximum.

Table A1. Difference in range ($\Delta R_{80\%}$), longitudinal Bragg peak width $\Delta W_{80\%}$ and difference in beam centre (Δx) and width ($\Delta \sigma_x$) at 80% of $R_{80\%}$ between analytical and MC results. Results for 0, 0.5 and 1.5 T and 70, 170 and 228 MeV are listed, as well as the maximum observed difference for each magnetic field strength.

Magnetic field	Energy [MeV]	$\Delta R_{80\%}$ [mm]	$\Delta W_{80\%}$ [mm]	Δx [mm]	$\Delta \sigma_x$ [mm]
0 T	70	−0.1	−0.2	–	0.4
	170	−0.3	−0.3	–	−0.2
	229	−0.5	−0.5	–	−1.6
	max	−0.7	−0.6	–	−2.2
0.5 T	70	−0.1	−0.2	0.1	0.3
	170	−0.3	−0.3	<0.1	−0.2
	229	−0.5	−0.4	0.1	−1.1
	max	−0.6	−0.4	−1.2	−1.7
1.5 T	70	−0.1	−0.2	0.3	0.5
	170	−0.3	0.1	0.2	−0.2
	229	−0.5	0.2	−0.4	−0.7
	max	−0.7	0.7	1.2	−2.3

analytical approach and MC simulation in the range $\Delta R_{80\%}$, Bragg peak width $\Delta W_{80\%}$, the beam deflection Δx and beam width $\Delta \sigma_x$ are listed in table A1. A sub-millimetre accuracy in the range $R_{80\%}$ and longitudinal Bragg peak width $W_{80\%}$ was achieved even for 1.5 T. The lateral shift agreed within 1.2 mm for all energies and both

magnetic field strength. Slightly larger differences in the lateral beam width σ_x up to 2.3 mm were observed also without magnetic field.

Appendix B. Benchmarking of algorithm for single pencil beams in different materials

The analytical dose calculation algorithm was further validated against MC in different homogeneous materials. For the lowest densities (−700 and −100 HU) a phantom of size 50 × 30 × 5 cm^3 was used, while for the higher densities (200, 300 and 1000 HU) 35 × 20 × 5 cm^3 was used. Dose distributions were computed with a resolution of 1 × 1 × 1 mm^3.

The differences in range ($\Delta R_{80\%}$) and the beam deflection (Δx) between the analytical approach and MC simulation are listed in table B1. Excellent agreement in the range can be observed with and without magnetic field, achieving sub-millimetre accuracy. Moreover, for all studied materials the beam bending was found to be very similar for the analytical approach and MC simulations, with a maximum deviation Δx of 2 mm.

Table B1. Difference in range ($\Delta R_{80\%}$) and difference in beam centre at 80% of $R_{80\%}$ (Δx) between analytical and MC results. Results for different materials, magnetic field strengths and energies are listed. For −700 HU results are only listed for 70 MeV, as for 170 MeV and 229 MeV the Bragg peak is outside of phantom due to the low density.

		0 T	0.5 T		1.5 T	
Material [HU]	Energy [MeV]	$\Delta R_{80\%}$ [mm]	$\Delta R_{80\%}$ [mm]	Δx [mm]	$\Delta R_{80\%}$ [mm]	Δx [mm]
−700	70	−0.6	−0.6	−0.1	−0.5	0.2
−100	70	<0.1	<0.1	0.1	0.1	<0.1
	170	−0.1	−0.1	−0.1	−0.1	0.1
	229	−0.4	−0.4	−1.0	−0.3	−1.0
200	70	<0.1	<0.1	−0.1	<0.1	0.1
	170	−0.2	−0.2	−0.1	−0.3	−0.2
	229	−0.4	−0.3	−1.0	−0.3	<0.1
300	70	−0.1	−0.1	−0.9	−0.1	0.1
	170	−0.2	−0.3	−0.8	−0.2	−0.1
	229	−0.3	−0.3	−1.0	−0.3	<0.1
1000	70	−0.4	−0.4	<0.1	−0.4	0.1
	170	−0.2	−0.2	−0.4	−0.1	−0.5
	229	<0.1	<0.1	−2.0	<0.1	−1.0

ORCID iDs

Alisha Duetschler https://orcid.org/0000-0001-5121-8032
Ye Zhang https://orcid.org/0000-0003-1608-4467

References

Agostinelli S *et al* 2003 Geant4–a simulation toolkit *Nucl. Instrum. Methods Phys. Res.* A **506** 250–303
Allison J *et al* 2006 Geant4 developments and applications *IEEE Trans. Nucl. Sci.* **53** 270–8
Allison J *et al* 2016 Recent developments in Geant4 *Nucl. Instrum. Methods Phys. Res.* A **835** 186–225
Boye D, Lomax T and Knopf A 2013a Mapping motion from 4D-MRI to 3D-CT for use in 4D dose calculations: a technical feasibility study *Med. Phys.* **40** 61702
Boye D, Samei G, Schmidt J, Székely G and Tanner C 2013b Population based modeling of respiratory lung motion and prediction from partial information *Medical Imaging 2013: Image Processing* vol 8669SPIE86690U
Bragg W H and Kleeman R 1905 XXXIX. On the α particles of radium, and their loss of range in passing through various atoms and molecules *London, Edinburgh, Dublin Phil. Mag. J. Sci.* **10** 318–40
Burigo L N and Oborn B M 2019 MRI-guided proton therapy planning: accounting for an inline MRI fringe field *Phys. Med. Biol.* **64** 215015
Burigo L N and Oborn B M 2021 Integrated MRI-guided proton therapy planning: accounting for the full MRI field in a perpendicular system *Med. Phys.* **49** 1853–73
Duetschler A, Prendi J, Safai S, Weber D C, Lomax A J and Zhang Y 2023 Limitations of phase-sorting based pencil beam scanned 4D proton dose calculations under irregular motion *Phys. Med. Biol.* **68** 015015
Faddegon B, Ramos-Mendez J, Schuemann J, McNamara A, Shin J, Perl J and Paganetti H 2020 The TOPAS tool for particle simulation, a monte carlo simulation tool for physics, biology and clinical research *Phys. Med.* **72** 114–21
Fuchs H, Moser P, Gröschl M and Georg D 2017 Magnetic field effects on particle beams and their implications for dose calculation in MR-guided particle therapy *Med. Phys.* **44** 1149–56

Fuchs H, Padilla-Cabal F, Oborn B M and Georg D 2022 Commissioning a beam line for MR-guided particle therapy assisted by in silico methods *Med. Phys.* **50** 1019–28
Gantz S, Hietschold V and Hoffmann A L 2020 Characterization of magnetic interference and image artefacts during simultaneous in-beam MR imaging and proton pencil beam scanning *Phys. Med. Biol.* **65** 215014
Gantz S, Schellhammer S M and Hoffmann A L 2021 Image performance characterization of an in-beam low-field magnetic resonance imaging system during static proton beam irradiation *IEEE Trans. Radiat. Plasma Med. Sci.* **6** 271–81
Hackett S L, Van Asselen B, Wolthaus J W, Bluemink J J, Ishakoglu K, Kok J, Lagendijk J J and Raaymakers B W 2018 Spiraling contaminant electrons increase doses to surfaces outside the photon beam of an MRI-linac with a perpendicular magnetic field *Phys. Med. Biol.* **63** 095001
Hartman J, Kontaxis C, Bol G H, Frank S J, Lagendijk J J W, van Vulpen M and Raaymakers B W 2015 Dosimetric feasibility of intensity modulated proton therapy in a transverse magnetic field of 1.5 T *Phys. Med. Biol.* **60** 5955–69
Hoffmann A, Oborn B, Moteabbed M, Yan S, Bortfeld T, Knopf A, Fuchs H, Georg D, Seco J, Spadea M F, Jäkel O, Kurz C and Parodi K 2020 MR-guided proton therapy: a review and a preview *Radiat. Oncol.* **15** 129
Jia X, Schümann J, Paganetti H and Jiang S B 2012 GPU-based fast Monte Carlo dose calculation for proton therapy *Phys. Med. Biol.* **57** 7783–97
Krieger M, Klimpki G, Fattori G, Hrbacek J, Oxley D, Safai S, Weber D C, Lomax A J and Zhang Y 2018 Experimental validation of a deforming grid 4D dose calculation for PBS proton therapy *Phys. Med. Biol.* **63** 055005
Kurz C, Landry G, Resch A F, Dedes G, Kamp F, Ganswindt U, Belka C, Raaymakers B W and Parodi K 2017 A Monte-Carlo study to assess the effect of 1.5 T magnetic fields on the overall robustness of pencil-beam scanning proton radiotherapy plans for prostate cancer *Phys. Med. Biol.* **62** 8470–82
Lee H, Shin J, Verburg J M, Bobić M, Winey B, Schuemann J and Paganetti H 2022 MOQUI: an open-source GPU-based Monte Carlo code for proton dose calculation with efficient data structure *Phys. Med. Biol.* **67** 174001
Lomax A 1999b Intensity modulation methods for proton radiotherapy *Phys. Med. Biol.* **44** 185–205
Lomax A J, Bortfeld T, Goitein G, Debus J, Dykstra C, Tercier P A, Coucke P A and Mirimanoff R O 1999a A treatment planning inter-comparison of proton and intensity modulated photon radiotherapy *Radiother. Oncol.* **51** 257–71
Lühr A, Burigo L N, Gantz S, Schellhammer S M and Hoffmann A L 2019 Proton beam electron return effect: Monte Carlo simulations and experimental verification *Phys. Med. Biol.* **64**
Lysakovski P, Ferrari A, Tessonnier T, Besuglow J, Kopp B, Mein S, Haberer T, Debus J and Mairani A 2021 Development and benchmarking of a Monte Carlo dose engine for proton radiation therapy *Front. Phys.* **9** 655
Malkov V N, Hackett S L, Wolthaus J W, Raaymakers B W and Van Asselen B 2019 Monte Carlo simulations of out-of-field surface doses due to the electron streaming effect in orthogonal magnetic fields *Phys. Med. Biol.* **64** 115029
Matter M, Nenoff L, Marc L, Weber D C, Lomax A J and Albertini F 2020 Update on yesterday's dose-Use of delivery log-files for daily adaptive proton therapy (DAPT) *Phys. Med. Biol.* **65** 195011
Matter M, Nenoff L, Meier G, Weber D C, Lomax A J and Albertini F 2019 Intensity modulated proton therapy plan generation in under ten seconds *Acta Oncol.* **58** 1435–9
Moteabbed M, Schuemann J and Paganetti H 2014 Dosimetric feasibility of real-time MRI-guided proton therapy *Med. Phys.* **41** 111713
Mutic S and Dempsey J F 2014 The viewray system: magnetic resonance-guided and controlled radiotherapy *Semin. Radiat. Oncol.* **24** 196–9
Nenoff L, Matter M, Charmillot M, Krier S, Uher K, Weber D C, Lomax A J and Albertini F 2021 Experimental validation of daily adaptive proton therapy *Phys. Med. Biol.* **66** 205010
Nenoff L *et al* 2020 Daily adaptive proton therapy: is it appropriate to use analytical dose calculations for plan adaption? *Int. J. Radiat. Oncol.***Biol.***Phys.* **107** 747–55
Oborn B M, Dowdell S, Metcalfe P E, Crozier S, Mohan R and Keall P J 2015 Proton beam deflection in MRI fields: implications for MRI-guided proton therapy *Med. Phys.* **42** 2113–24
Oborn B M, Dowdell S, Metcalfe P E, Crozier S, Mohan R and Keall P J 2017 Future of medical physics: real-time MRI-guided proton therapy *Med. Phys.* **44** e77–90
Oborn B M, Metcalfe P E, Butson M J and Rosenfeld A B 2009 High resolution entry and exit Monte Carlo dose calculations from a linear accelerator 6 MV beam under the influence of transverse magnetic fields *Med. Phys.* **36** 3549–59
Padilla-Cabal F, Alejandro Fragoso J, Franz Resch A, Georg D and Fuchs H 2020b Benchmarking a GATE/Geant4 Monte Carlo model for proton beams in magnetic fields *Med. Phys.* **47** 223–33
Padilla-Cabal F, Georg D and Fuchs H 2018 A pencil beam algorithm for magnetic resonance image-guided proton therapy *Med. Phys.* **45** 2195–204
Padilla-Cabal F, Kuess P, Georg D, Palmans H, Fetty L and Fuchs H 2019 Characterization of EBT3 radiochromic films for dosimetry of proton beams in the presence of magnetic fields *Med. Phys.* **46** 3278–84
Padilla-Cabal F, Resch A F, Georg D and Fuchs H 2020a Implementation of a dose calculation algorithm based on Monte Carlo simulations for treatment planning towards MRI guided ion beam therapy *Phys. Med.* **74** 155–65
Park J M, Shin K H, Kim J I, Park S Y, Jeon S H, Choi N, Kim J H and Wu H G 2018 Air-electron stream interactions during magnetic resonance IGRT: skin irradiation outside the treatment field during accelerated partial breast irradiation *Strahlentherapie und Onkologie* **194** 50–9
Pedroni E *et al* 2004 The PSI Gantry 2: a second generation proton scanning gantry *Z. Med. Phys.* **14** 25–34
Pedroni E, Scheib S, Böhringer T, Coray A, Grossmann M, Lin S and Lomax A 2005 Experimental characterization and physical modelling of the dose distribution of scanned proton pencil beams *Phys. Med. Biol.* **50** 541–61
Perl J, Shin J, Schumann J, Faddegon B and Paganetti H 2012 TOPAS: an innovative proton Monte Carlo platform for research and clinical applications *Med. Phys.* **39** 6818–37
Pham T T, Whelan B, Oborn B M, Delaney G P, Vinod S, Brighi C, Barton M and Keall P 2022 Magnetic resonance imaging (MRI) guided proton therapy: a review of the clinical challenges, potential benefits and pathway to implementation *Radiother. Oncol.* **170** 37–47
Raaijmakers A J E, Raaymakers B W and Lagendijk J J W 2005 Integrating a MRI scanner with a 6 MV radiotherapy accelerator: dose increase at tissue-air interfaces in a lateral magnetic field due to returning electrons *Phys. Med. Biol.* **50** 1363–76
Raaijmakers A J E, Raaymakers B W and Lagendijk J J W 2008 Magnetic-field-induced dose effects in mr-guided radiotherapy systems: dependence on the magnetic field strength *Phys. Med. Biol.* **53** 909–23
Raaijmakers A J, Raaymakers B W, van der Meer S and Lagendijk J J 2007 Integrating a MRI scanner with a 6 MV radiotherapy accelerator: impact of the surface orientation on the entrance and exit dose due to the transverse magnetic field *Phys. Med. Biol.* **52** 929–39
Raaymakers B W *et al* 2017 First patients treated with a 1.5 T MRI-Linac: clinical proof of concept of a high-precision, high-field MRI guided radiotherapy treatment *Phys. Med. Biol.* **62** L41–50

Raaymakers B W, Raaijmakers A J E and Lagendijk J J W 2008 Feasibility of MRI guided proton therapy: magnetic field dose effects *Phys. Med. Biol.* **53** 5615–22

Safai S, Bula C, Meer D and Pedroni E 2012 Improving the precision and performance of proton pencil beam scanning *Transl. Cancer Res.* **1** 196–206

Santos D M, Wachowicz K, Burke B and Fallone B G 2019 Proton beam behavior in a parallel configured MRI-proton therapy hybrid: effects of time-varying gradient magnetic fields *Med.Phys.* **46** 822–38

Schaffner B, Pedroni E and Lomax A 1999 Dose calculation models for proton treatment planning using a dynamic beam delivery system: an attempt to include density heterogeneity effects in the analytical dose calculation *Phys. Med. Biol.* **44** 27–41

Schellhammer S M, Gantz S, Lühr A, Oborn B M, Bussmann M and Hoffmann A L 2018b Technical note: experimental verification of magnetic field-induced beam deflection and Bragg peak displacement for MR-integrated proton therapy *Med. Phys.* **45** 3429–34

Schellhammer S M and Hoffmann A L 2017 Prediction and compensation of magnetic beam deflection in MR-integrated proton therapy: a method optimized regarding accuracy, versatility and speed *Phys. Med. Biol.* **62** 1548–64

Schellhammer S M, Hoffmann A L, Gantz S, Smeets J, van der Kraaij E, Quets S, Pieck S, Karsch L and Pawelke J 2018a Integrating a low-field open MR scanner with a static proton research beam line: proof of concept *Phys. Med. Biol.* **63** 23LT01

Schiavi A, Senzacqua M, Pioli S, Mairani A, Magro G, Molinelli S, Ciocca M, Battistoni G and Patera V 2017 Fred: a GPU-accelerated fast-Monte Carlo code for rapid treatment plan recalculation in ion beam therapy *Phys. Med. Biol.* **62** 7482–504

Soukup M, Fippel M and Alber M 2005 A pencil beam algorithm for intensity modulated proton therapy derived from Monte Carlo simulations *Phys. Med. Biol.* **50** 5089–104

Souris K, Lee J A and Sterpin E 2016 Fast multipurpose Monte Carlo simulation for proton therapy using multi- and many-core CPU architectures *Med. Phys.* **43** 1700–12

Van De Water S, Kreuger R, Zenklusen S, Hug E and Lomax A J 2009 Tumour tracking with scanned proton beams: assessing the accuracy and practicalities *Phys. Med. Biol.* **54** 6549–63

Wan Chan Tseung H, Ma J and Beltran C 2015 A fast GPU-based Monte Carlo simulation of proton transport with detailed modeling of nonelastic interactions *Med. Phys.* **42** 2967–78

Winterhalter C 2019 Protons do play dice: validating, implementing and applying Monte Carlo techniques for proton therapy *PhD Thesis* ETH Zürich

Winterhalter C *et al* 2018 Validating a Monte Carlo approach to absolute dose quality assurance for proton pencil beam scanning *Phys. Med. Biol.* **63** 175001

Winterhalter C, Meier G, Oxley D, Weber D C, Lomax A J and Safai S 2019b Log file based Monte Carlo calculations for proton pencil beam scanning therapy *Phys. Med. Biol.* **64** 035014

Winterhalter C *et al* 2019a Evaluation of the ray-casting analytical algorithm for pencil beam scanning proton therapy *Phys. Med. Biol.* **64** 065021

Wolf R and Bortfeld T 2012 An analytical solution to proton Bragg peak deflection in a magnetic field *Phys. Med. Biol.* **57** N329–37

Yang J, He P, Wang H, Sun G, Zheng H and Jia J 2020 An improved beam splitting method for intensity modulated proton therapy *Phys. Med. Biol.* **65** 185015

Zenklusen S M, Pedroni E and Meer D 2010 A study on repainting strategies for treating moderately moving targets with proton pencil beam scanning at the new gantry 2 at PSI *Phys. Med. Biol.* **55** 5103–21